

Topological surface state manipulation of magnetic damping and surface anisotropy in topological insulator/nonmagnet/CoFe heterostructures

Guanjie Wu,¹ Di Wu,¹ Yang Ren,² Q. Y. Jin,¹ and Zongzhi Zhang^{1,*}

¹Shanghai Ultra-Precision Optical Manufacturing Engineering Research Center and Key Laboratory of Micro and Nano Photonic Structures (MOE), Department of Optical Science and Engineering, Fudan University, Shanghai 200433, China

²School of Physics and Astronomy, Yunnan University, Kunming 650091, China



(Received 6 November 2020; accepted 5 January 2021; published 13 January 2021)

The recent advances of high spin-orbit torque efficiency in ferromagnetic/topological insulator (TI) structures hold great promise for the development of high-performance spintronic devices. However, the roles of spin-momentum-locked Dirac surface states (SSs) and the interfacial magnetic proximity effect (MPE) on dynamic magnetic properties are still under debate. Here, we quantitatively distinguish the manipulation effects of SSs and MPE on magnetic damping and surface anisotropy in TI/nonmagnet/CoFe heterostructures. We found that, in addition to the common spin pumping contribution stemming from SSs, damping enhancement also consists of an obvious MPE contribution to the TI/CoFe material system. Moreover, the increased surface magnetic anisotropy for the CoFe films grown on top of a TI layer is believed to arise mainly from the interfacial atomic intermixing. Our paper sheds light on the effects of SSs and MPE on magnetization dynamics, which offer exciting opportunities for developing TI-based spintronics.

DOI: [10.1103/PhysRevB.103.014419](https://doi.org/10.1103/PhysRevB.103.014419)

I. INTRODUCTION

Since the theoretical prediction in 2009 by Zhang *et al.*, three-dimensional topological insulators (TIs) with insulating bulk and conducting surface states (SSs), such as Bi₂Se₃, Bi₂Te₃, and Sb₂Te₃, have attracted much attention for potential applications in ultralow power and ultrafast spintronic devices [1–8]. Due to the unique spin-momentum-locked Dirac SSs, high-efficiency charge-to-spin current conversion has been theoretically predicted and experimentally demonstrated [1,9–11]. Therefore, as a promising high-efficiency spin current source, TIs were proposed to replace the traditional heavy metals (HMs) to exert strong spin-orbit torques (SOTs) acting on the adjacent ferromagnetic (FM) layer [12,13]. The SOT-driven magnetization switching has been demonstrated at room temperature (RT) in various TI/FM heterostructures [14,15], showing a critical switching current density as low as $\sim 10^5$ A/cm² [16–19]. It is believed that the ultrahigh SOT efficiency observed in the TI/FM bilayers is generally resulted from the helical Dirac SSs [20]. Nevertheless, it has been pointed out that the spin Hall effect in the TI bulk and Rashba effect at the TI/FM interface may also generate spin current and hence affect the SOT strength [21]. For instance, the SOT ratio was greatly improved at RT by inserting an interlayer of Ag at the interface between Bi₂Se₃ and CoFeB, which is primarily the result of the interfacial Rashba effect [22]. In addition, by tuning x in (Bi_{1-x}Sb_x)₂Te₃, it was found that the bulk charge current can also contribute to spin current via the ordinary spin Hall effect [23].

The TIs in contact with a FM layer can not only serve as a spin current source for SOT-driven magnetization switching

or persistent oscillation, but they are also a good spin sink layer [24]. Due to the interfacial inverse Edelstein effect associated with the strong spin-momentum-locking SSs, a large magnetic damping enhancement was reported in TI/FM structures via the spin pumping effect [25,26]. As a key parameter for realizing fast manipulation of magnetization states and low energy consumption in spintronic devices, the magnetic damping factor α of a FM is demonstrated to rely not only on the topological SSs but the bulk state of the adjacent TI layer as well, where the spin current pumped from the precessing FM layer dissipates. Nomura *et al.* found that, in TI/NiFe heterostructures, the absorption of spin current is dominated by the SSs of TI at low temperature, whereas it becomes comparable with that in the bulk state near RT [27]. Large interfacial in-plane (IP) magnetic anisotropy and enhanced magnetic damping were reported in Bi₂Se₃/yttrium iron garnet (YIG) structures, which reached a maximum when Bi₂Se₃ approached its two-dimensional limit, indicating that topological SSs play an important role [28]. It should be noted that magnetic order could be induced at the TI surface via the strong interfacial band hybridization between the metallic SSs of TI and the adjacent $3d$ transition metal (Co, Fe, and Ni), i.e., the magnetic proximity effect (MPE) [29]. Like the HM/FM system [30–32], magnetic exchange coupling between the FM layer and the induced magnetism at the TI surface could result in an additional magnetic damping as well [33]. However, in previously published papers, the damping contribution related to MPE was considered negligible at RT, which is probably due to the much lower Curie temperature of the induced magnetic order at the TI surface [34–36].

Since the magnetic surface anisotropy and additional damping contributions are all closely associated with the topological Dirac SSs and interfacial coupling interaction, understanding the role of the TI/FM interface is crucial

*zzzhang@fudan.edu.cn

for achieving ultrafast control of magnetization orientation at reduced power consumption. However, the MPE effect has not been clarified yet. Moreover, the magnetic precession and damping behaviors in TI/FM heterostructures were largely investigated by the FM resonance method so far. From the practical application point of view, it is essential to detect the transient response of spin dynamics in the time domain by using the time-resolved magneto-optical Kerr effect (TR-MOKE) approach [37–42]. As a result, in this paper, we perform a systematic study on the laser-induced magnetization dynamics in TI/nonmagnetic (NM)/CoFe heterostructures by using the TR-MOKE technique, where different TI layers including Bi_2Te_3 , Sb_2Te_3 , and Cr-doped $(\text{Cr}_{0.2}\text{Bi}_{0.24}\text{Sb}_{0.56})_2\text{Te}_3$ are employed. By varying the NM (Ta or Al) interlayer material, thickness, and measurement temperature, the TI/FM exchange coupling strength and spin pumping effect are well adjusted, from which the manipulation effects of SSs and MPE on magnetic damping and surface anisotropy are clearly distinguished.

II. EXPERIMENTAL METHOD

The TI films were grown by using a chemical vapor deposition method. After the deposition of the TI, samples were then immediately transferred into the sputtering system for magnetic layer deposition. Three series of samples in a structure of sapphire/TI (6)/Ta($t_{\text{Ta}} = 0\text{--}2.0$)/ $\text{Co}_{80}\text{Fe}_{20}$ (8)/Al (5) (layer thickness in nanometers) were firstly prepared, where the TI material was Bi_2Te_3 , Sb_2Te_3 , or $(\text{Cr}_{0.2}\text{Bi}_{0.24}\text{Sb}_{0.56})_2\text{Te}_3$. To improve the dynamic magnetic signal-to-noise ratio, we also prepared two other series of samples of $\text{SiO}_2/\text{Bi}_2\text{Te}_3$ (20)/Ta or Al ($0\text{--}2.0$)/ $\text{Co}_{80}\text{Fe}_{20}$ (20)/Al (5) with a thicker CoFe layer. The NM Al or Ta interlayer was employed to modulate the interfacial TI/FM coupling strength. In addition, for the convenience of comparison, some reference samples of SiO_2/Ta or Al($t_{\text{NM}} = 0\text{--}2.0$)/ $\text{Co}_{80}\text{Fe}_{20}$ (20)/Al (5) without any TI underlayer were also fabricated. The static magnetic properties were measured by a vibrating sample magnetometer (VSM), whereas the dynamic TR-MOKE measurements were achieved by using a pulsed Ti:sapphire laser with a central wavelength of 800 nm, a pulse duration of 150 fs, and a repetition rate of 1000 Hz. An intense pump pulse beam with a fluence of approximately 1.0 mJ/cm^2 was used to excite the dynamic magnetization behaviors, and the transient MOKE signal was detected by a weak probe pulse of approximately 0.05 mJ/cm^2 , which was time delayed with respect to the pump beam. The pump and probe laser beams were at almost perpendicular incidence, with spot diameters of about 1.0 and 0.2 mm, respectively. During the TR-MOKE measurement, a variable magnetic field H was applied at a tilted angle of 19° with respect to the film plane to drive the magnetization away from its easy plane [43,44]. In this paper, the TR-MOKE measurement temperature varied in the range of 80–300 K.

III. RESULTS AND DISCUSSION

Figure 1(a) shows the layer structure of the composite films. The pump and probe beams are spatially overlapped on the sample surface to locally excite and probe the

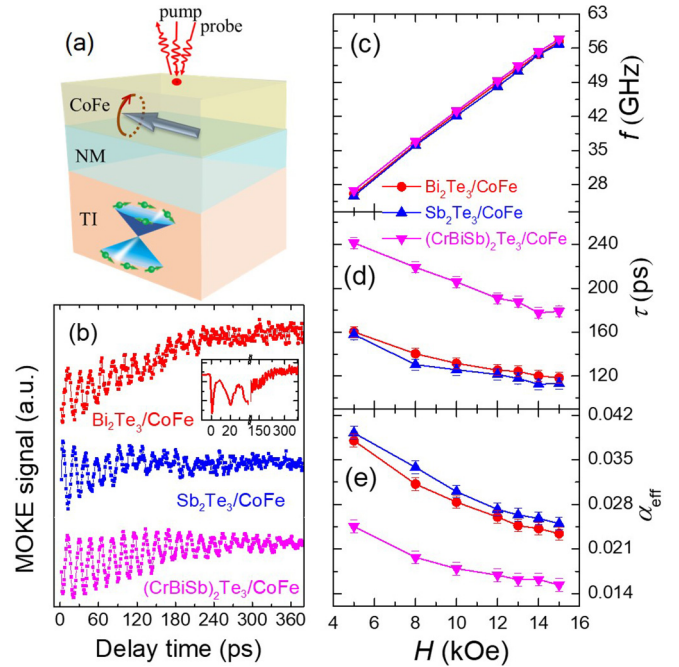


FIG. 1. (a) Illustration of the sample layer structure and pump-probe laser beams. (b) The typical time-resolved magneto-optical Kerr effect (TR-MOKE) curves for the samples of Bi_2Te_3 , Sb_2Te_3 , and $(\text{CrBiSb})_2\text{Te}_3$ (6)/CoFe (8) under $H = 15\text{ kOe}$. The inset displays a complete transient TR-MOKE curve for the sample of $\text{Bi}_2\text{Te}_3/\text{CoFe}$. The field dependences of the fitted (c) precession frequency f , (d) decay time τ , and (e) the calculated effective magnetic damping factor α_{eff} .

magnetization dynamics. Figure 1(b) presents the typical dynamic TR-MOKE curves of Bi_2Te_3 , Sb_2Te_3 , and $(\text{CrBiSb})_2\text{Te}_3$ (6)/CoFe (8) samples measured at $H = 15\text{ kOe}$. The inset of Fig. 1(b) displays a complete transient TR-MOKE curve for the sample of $\text{Bi}_2\text{Te}_3/\text{CoFe}$ upon laser excitation, which includes an ultrafast demagnetization process occurring within 1 ps and a subsequent damped magnetization precession process lasting for several hundred picoseconds. To avoid the influence of a demagnetization signal on the analyses of precession behavior, in Fig. 1(b), we only show the recovery process for the delay time ranging from 2 to 380 ps. By fitting these dynamic Kerr signals with an exponentially damped sine function of [45]

$$\theta_k = a + b \exp\left(\frac{t}{t_0}\right) + c \sin(2\pi ft + \varphi) \exp\left(-\frac{t}{\tau}\right), \quad (1)$$

the precession frequency f and decay time τ in the third term can be derived, which are shown in Figs. 1(c) and 1(d) as a function of H , respectively. Based on the fitted f and τ , the effective damping factor α_{eff} are calculated according to the approximate equation of $\alpha_{\text{eff}} = 1/(2\pi f\tau)$ [46], which includes both the intrinsic and extrinsic damping contributions. As shown in Fig. 1(e), α_{eff} decreases significantly with the increase in H and becomes nearly saturated at $H > 12\text{ kOe}$, implying that the extrinsic damping that stems from inhomogeneous magnetic distributions plays a major role at low fields. To clearly illustrate the role of TI underlayers on α , the influence of magnetic inhomogeneities

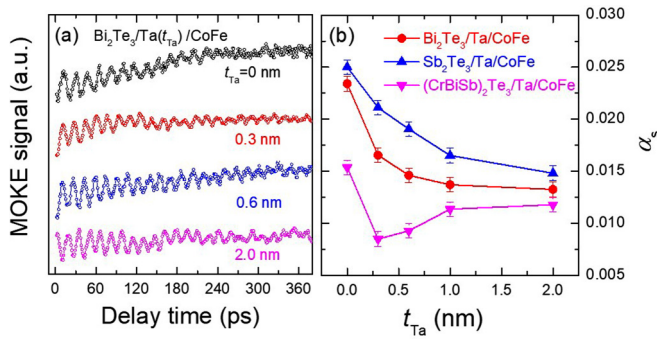


FIG. 2. (a) The time-resolved magneto-optical Kerr effect (TR-MOKE) curves for the samples of Bi_2Te_3 (6)/Ta (t_{Ta})/CoFe (8) measured under $H = 15$ kOe. (b) The saturated damping factor α_s as a function of t_{Ta} for the samples of TI (6)/Ta (t_{Ta})/CoFe (8).

should be suppressed. For this, the obtained field-dependent α_{eff} curves are fitted using a decaying exponential function of $\alpha_{\text{eff}} = \alpha_s + \alpha_{\text{ex}0} \exp(-H/H_0)$ [42], where α_s corresponds to the saturated damping at an infinite H . The fitted α_s are 0.023, 0.025, and 0.015 for the CoFe (8) films in contact with Bi_2Te_3 , Sb_2Te_3 , and $(\text{CrBiSb})_2\text{Te}_3$, respectively. Considering that all the CoFe samples have the same thickness and the same capping layer, the observed α_s difference should be mainly related to the spin current absorption in the TI underlayer. As compared with the heterostructures of Bi_2Te_3 and Sb_2Te_3 /CoFe with spin-momentum-locked gapless helical SSs, the $(\text{CrBiSb})_2\text{Te}_3$ /CoFe sample exhibits a significantly smaller α_s , which can be attributed to the weakened nontrivial metallic SSs due to the energy gap opening by magnetic doping [47,48]. Moreover, due to the relatively stronger topological SSs of Sb_2Te_3 [25], the α_s value is slightly higher than that of the Bi_2Te_3 case. It should be mentioned that the MPE contribution to damping cannot be simply ruled out in our TI/FM structure, since the Curie temperature of CoFe magnetic layer is as high as 1200 K [49]. That means, it is highly likely that the observed damping enhancement consists of both the MPE contribution caused by magnetic coupling at

the TI/FM interface and the spin pumping contribution that mainly stems from the SSs of TI.

We further examined the effect of the NM Ta interlayer on the spin pumping damping. Figure 2(a) shows the typical TR-MOKE curves for the samples of Bi_2Te_3 (6)/Ta ($t_{\text{Ta}} = 0-2.0$)/CoFe (8) with various Ta interlayer thicknesses, suggesting an obvious modulation of t_{Ta} on the precession lifetime. The saturated damping factor α_s is derived and shown in Fig. 2(b) as a function of t_{Ta} for the samples with different TI materials. Apparently, the variation trends of Bi_2Te_3 and Sb_2Te_3 samples are quite similar; both decrease monotonically with the increase in t_{Ta} , which can be interpreted as the result of reduced spin-mixing conductance as the TI/FM interface is replaced by Ta/FM. Nevertheless, the strong damping reduction may include the decreased MPE contribution since it is known that the induced magnetization at the TI surface and its magnetic coupling with CoFe will be suppressed by the insertion of Ta layer.

Interestingly, different from the monotonic decreasing trend of Bi_2Te_3 and Sb_2Te_3 , the α_s value of $(\text{CrBiSb})_2\text{Te}_3$ /CoFe firstly decreases and then increases with the increase in t_{Ta} . We consider that the initial significant reduction down to 0.008 at $t_{\text{Ta}} = 0.3$ nm comes from the reduced interfacial spin-mixing conductance, while the subsequent enhancement corresponds to the spin pumping damping induced by the Ta layer [50,51]. This variation behavior confirms the weakened spin-momentum-locking SSs in the $(\text{CrBiSb})_2\text{Te}_3$ layer, which can be easily destroyed by a Ta neighbor layer as thin as 0.3 nm. Note that the difference of α_s between the three kinds of samples gradually decreases with the increase in t_{Ta} . It is expected that, when t_{Ta} exceeds its spin diffusion length of $\lambda_{\text{Ta}} \sim 3.0$ nm [52,53], α_s will eventually become equal since the pumped spin current dissipates entirely within the Ta interlayer, and the SSs of TI would not play any role.

To recognize the MPE influences on magnetic damping and other magnetic properties in the TI/FM system, we then prepared some heterostructures of $\text{SiO}_2/\text{Bi}_2\text{Te}_3$ (20)/Ta or Al (0-2)/CoFe (20), where two different interlayers of Ta and Al were employed. As compared with Ta, the spin

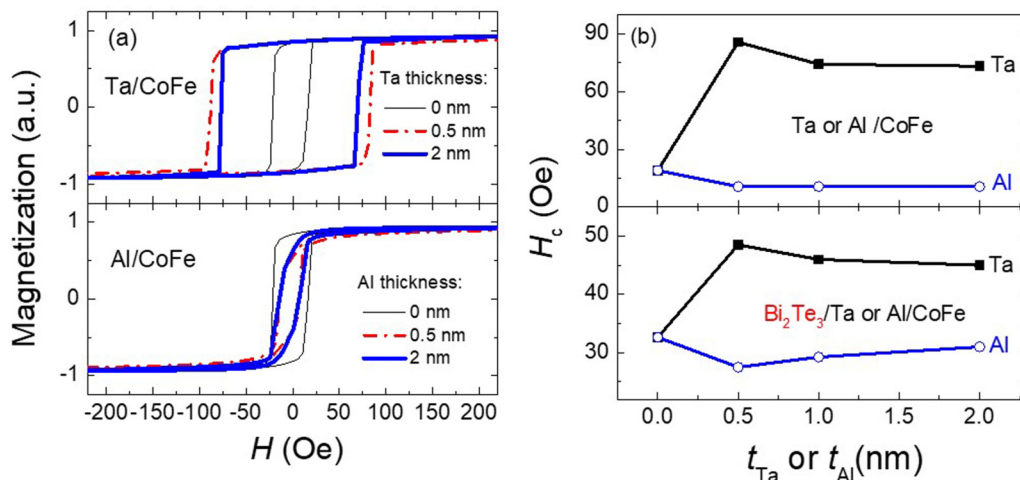


FIG. 3. (a) The typical in-plane magnetic hysteresis loops for SiO_2/Ta or Al (t_{NM})/CoFe (20) samples. (b) Magnetic coercivity H_c versus the Ta (t_{Ta}) or Al (t_{Al}) interlayer thicknesses for the samples of SiO_2/Ta or Al/CoFe (20) and $\text{SiO}_2/\text{Bi}_2\text{Te}_3$ (20)/Ta or Al/CoFe (20).

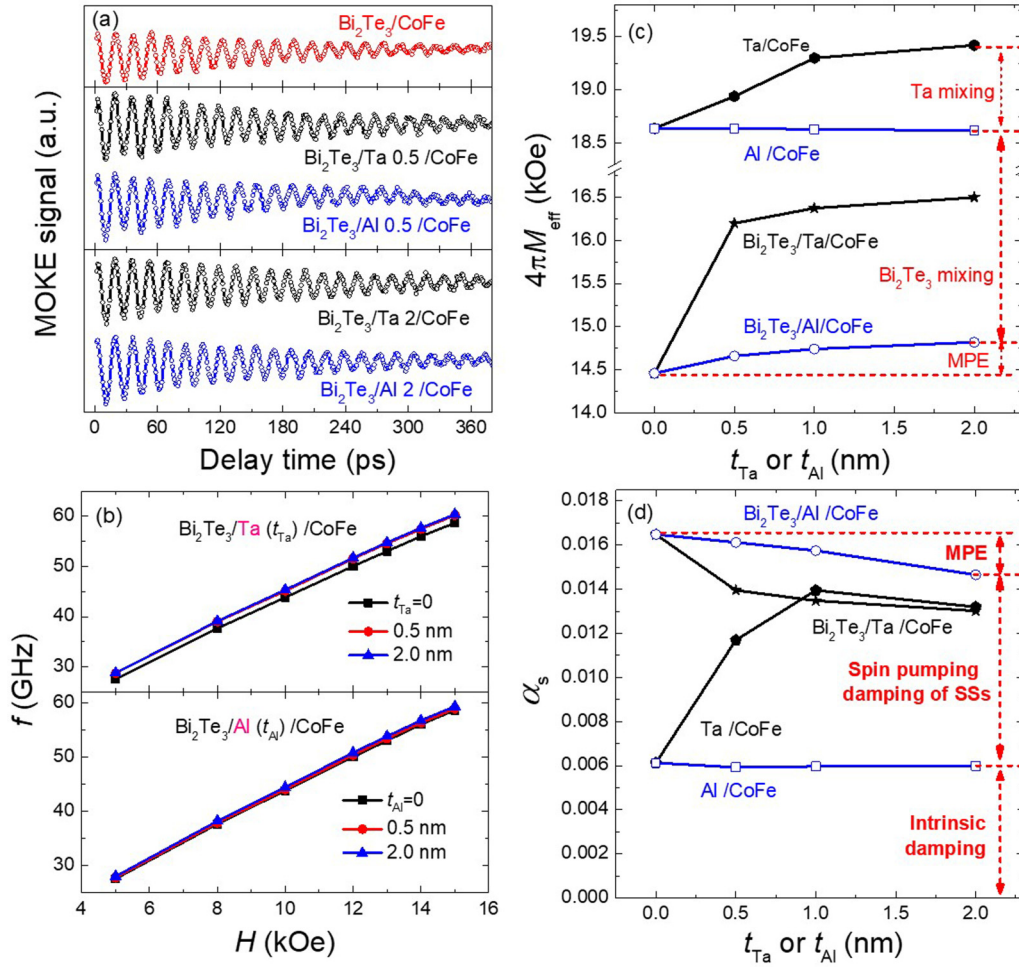


FIG. 4. (a) The typical time-resolved magneto-optical Kerr effect (TR-MOKE) curves under $H = 15$ kOe for the samples of $\text{SiO}_2/\text{Bi}_2\text{Te}_3$ (20)/Ta or Al/CoFe (20) with different interlayer thicknesses and (b) the corresponding field-dependent precession frequencies. The effective saturation magnetization $4\pi M_{\text{eff}}$ and α_s as a function of t_{Ta} or t_{Al} for the samples of (c) SiO_2/Ta or Al/CoFe (20) and (d) $\text{SiO}_2/\text{Bi}_2\text{Te}_3$ (20)/Ta or Al/CoFe (20). Note that the $4\pi M_{\text{eff}}$ values were derived by fitting the field-dependent frequency curves shown in Fig. 4(b).

diffusion length of Al is rather long due to the weak spin-orbit coupling strength [52], which means the 0–2 nm Al interlayer is nearly transparent for spin current transmission. It should be mentioned that, considering the laser penetration depth for transition metal films is approximately 10–20 nm [37,54], here, the CoFe layer thickness is increased up to 20 nm to improve the magnetic signal response. As seen in Figs. 1(b) and 2(a), the TR-MOKE curves of 8-nm-thick CoFe thin films grown on top of a TI layer have a rather poor magnetic signal-to-noise ratio due to the severe influence of laser-induced carrier dynamics of the TI layer [55,56]. Figure 3(a) shows the typical IP magnetic hysteresis loops for the reference samples of SiO_2/Ta or Al (0, 0.5, and 2)/CoFe (20) without the TI underlayer; they all exhibit definite IP magnetic anisotropy but with quite different magnetic coercivity H_c . Figure 3(b) displays the varying trend of H_c as a function of t_{Ta} or t_{Al} thickness. Apparently, no matter whether the TI underlayer exists or not, the insertion of a thin Ta layer could significantly enhance the H_c value, which can be ascribed to the enhancement of IP anisotropy [57,58]. The slight decline of H_c with further increase in t_{Ta} is probably due to the

weakening of the domain wall pinning effect, considering the amorphous nature of Ta. In contrast, for the samples with an Al interlayer, H_c changes rather slightly, suggesting that the magnetic properties of CoFe is almost undisturbed by the Al interlayer.

Figure 4(a) displays the TR-MOKE curves measured at $H = 15$ kOe for the samples of Bi_2Te_3 (20)/Ta or Al/CoFe (20) with various interlayer thicknesses. As compared with the 8-nm-thick CoFe films, the MOKE signal is greatly improved, exhibiting a good exponentially damped oscillation behavior. The corresponding f - H curves are shown in Fig. 4(b), which were fitted with the following formula according to the uniform Kittel precession model [45]:

$$2\pi f = \gamma \sqrt{H_1 H_2}, \quad (2)$$

where $\gamma = \gamma_e g/2$ is the gyromagnetic ratio with $\gamma_e = 1.76 \times 10^7$ Hz/Oe, g is the Lande's splitting factor and is taken to be 2.16 for CoFe [59]. Here, H_1 and H_2 are defined as $H_1 = H \cos(\theta - \theta_H) - 4\pi M_{\text{eff}} \cos 2\theta$ and $H_2 = H \cos(\theta - \theta_H) - 4\pi M_{\text{eff}} \cos^2 \theta$, respectively. The magnetization equilibrium angle θ can be determined according to the relation of

$2H \sin(\theta - \theta_H) = 4\pi M_{\text{eff}} \sin 2\theta$, and the effective magnetization $4\pi M_{\text{eff}}$ is defined by the following expression:

$$4\pi M_{\text{eff}} = 4\pi M_s - \frac{2K_s}{M_s t_{\text{CoFe}}}, \quad (3)$$

where K_s denotes the surface anisotropy energy constant and M_s is the saturation magnetization. The fitted $4\pi M_{\text{eff}}$ values for the four series of samples, Ta/CoFe, Al/CoFe, $\text{Bi}_2\text{Te}_3/\text{Ta}/\text{CoFe}$, and $\text{Bi}_2\text{Te}_3/\text{Al}/\text{CoFe}$ are displayed in Fig. 4(c). Apparently, the $4\pi M_{\text{eff}}$ value of CoFe varies significantly with the underlayer material and thickness. It is around 18.6 kOe for the single CoFe film, which decreases dramatically down to 14.5 kOe when growing on top of Bi_2Te_3 . Considering that M_s changes little, the decreased $4\pi M_{\text{eff}}$ of ~ 4.9 kOe suggests an enhanced perpendicular magnetic anisotropy (PMA) according to Eq. (3), which has been verified by the IP and out-of-plane (OP) magnetic hysteresis loops (see Fig. 6 in Appendix for details). Nevertheless, it is difficult to tell whether the observed strong enhancement in PMA arises from MPE (orbital hybridization between the SSs of Bi_2Te_3 and FeCo 3d electrons) [24,27,34,35] or from atomic intermixing at the $\text{Bi}_2\text{Te}_3/\text{CoFe}$ interface [60] since both mechanisms can result in the change of magnetic anisotropy. To elucidate this, we should analyze the results of $4\pi M_{\text{eff}}$ versus t_{Ta} or t_{Al} . The increase in $4\pi M_{\text{eff}}$ for the Ta/CoFe series suggests a decreased K_s (or an increased IP magnetic anisotropy), which should be caused by interfacial intermixing of Ta with CoFe atoms. In sharp contrast, like the varying tendency of H_c , the $4\pi M_{\text{eff}}$ value of Al/CoFe again keeps unchanged with the increase in t_{Al} . Therefore, since the Al interlayer would not affect magnetic anisotropy but can isolate the interfacial coupling, we can attribute the small $4\pi M_{\text{eff}}$ increase in ~ 0.36 kOe between $\text{Bi}_2\text{Te}_3/\text{CoFe}$ and $\text{Bi}_2\text{Te}_3/\text{Al}(2)/\text{CoFe}$ to the MPE contribution, while the observed strong reduction of ~ 4.2 kOe for the CoFe film in contact with Bi_2Te_3 arises mainly from the atomic intermixing between Bi_2Te_3 and CoFe. For clarity, these different contributions to $4\pi M_{\text{eff}}$ are indicated in Fig. 4(c).

From the Al interlayer thickness independence of H_c and $4\pi M_{\text{eff}}$, we know that Al/CoFe serves as a good control sample structure, which can be utilized to clarify the physical origin of the magnetic damping factor in the TI/FM system. Figure 4(d) shows the obtained saturated damping values of α_s versus t_{Al} for both Al/CoFe and $\text{Bi}_2\text{Te}_3/\text{Al}/\text{CoFe}$ series. For the single CoFe film deposited directly on top of the SiO_2 substrate, the spin pumping contribution is negligible since the pumped spin current is completely reflected, leading to the smallest α_s of 0.006, which can be taken as the intrinsic damping of CoFe films. Moreover, we notice that α_s of Al/CoFe stays unchanged as t_{Al} increases from 0 to 2 nm, which is indicative of the weak SOC interaction and hence much longer spin diffusion length of the Al layer [60]. By contrast, the α_s value of $\text{Bi}_2\text{Te}_3/\text{CoFe}$ is almost three times larger than the single CoFe film, indicating that the spin pumping damping induced by the SSs of TI is significant. Although the Al interlayer in $\text{Bi}_2\text{Te}_3/\text{Al}/\text{CoFe}$ would not affect the spin pumping damping, it can suppress the coupling between TI and FM, being responsible for the gradual weak drop induced by MPE. Apparently, the reduction of α_s for $\text{Bi}_2\text{Te}_3/\text{Ta}/\text{CoFe}$ with the increase in t_{Ta} is larger than the case of $\text{Bi}_2\text{Te}_3/\text{Al}/\text{CoFe}$,

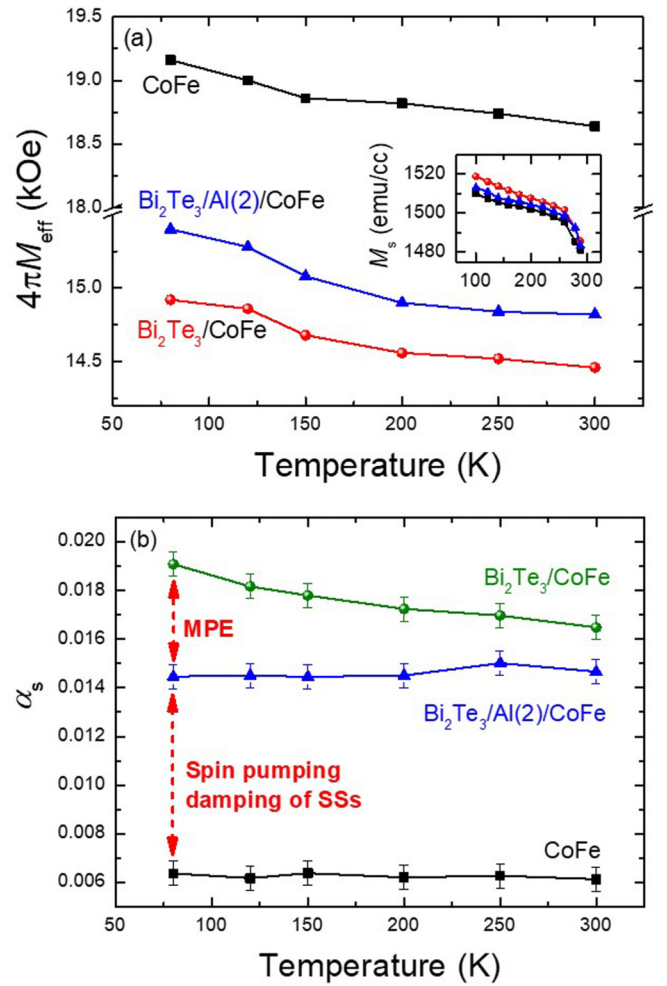


FIG. 5. The temperature dependences of $4\pi M_{\text{eff}}$ and α_s for the samples of (a) SiO_2/CoFe (20), $\text{SiO}_2/\text{Bi}_2\text{Te}_3$ (20)/CoFe (20) and (b) $\text{SiO}_2/\text{Bi}_2\text{Te}_3$ (20)/Al(2)/CoFe (20). The inset in (a) shows the corresponding M_s measured at different temperatures.

which has been ascribed to the spin current absorption in the Ta layer. It should be noted that the result of α_s versus t_{Ta} for both the Ta/CoFe and $\text{Bi}_2\text{Te}_3/\text{Ta}/\text{CoFe}$ series are also given in Fig. 4(d) for comparison. The nonmonotonic variation trend of α_s versus t_{Ta} for Ta/CoFe samples is like the relevant recent results reported experimentally and theoretically [61,62]. The initial increase is due to the intrinsic damping contributions from spin pumping effect and $d-d$ hybridization, as well as the extrinsic contribution from two-magnon scattering, while the subsequent reduction mainly results from the reduction of extrinsic contribution that largely vanishes for higher t_{Ta} .

We further performed the TR-MOKE measurements at various temperatures for the samples of single CoFe (20) film, Bi_2Te_3 (20)/CoFe (20) and Bi_2Te_3 (20)/Al (2)/CoFe (20). As shown in Fig. 5(a), the $4\pi M_{\text{eff}}$ values show a similar monotonic increasing trend with decreasing temperature for all the three samples. The amount of M_{eff} increase is very close to the increased M_s , as shown in the inset. It suggests that the M_s variation of CoFe dominates the temperature-dependent M_{eff} values, while the MPE contribution to the surface anisotropy K_s for the Bi_2Te_3 (20)/CoFe (20)

sample is very stable at low temperatures according to Eq. (3). Figure 5(b) shows the α_s values for these samples as a function of temperature. Just like the single CoFe (20) sample, the α_s value of Bi_2Te_3 (20)/Al(2)/CoFe (20) also stays almost constant with the decrease in temperature, indicating the spin pumping damping of the SSs is not sensitive to temperature [63]. In contrast, for the Bi_2Te_3 (20)/CoFe (20) sample, α_s increases gradually, which can be attributed to the enhanced MPE at low temperatures since the induced magnetic moments at the TI surface become more ordered.

IV. SUMMARY

In summary, magnetization dynamics in TI/Ta or Al/CoFe heterostructures have been systematically investigated by the TR-MOKE technique. As compared with Ta, the spin diffusion length of the Al interlayer is rather long. By comparing the different interlayer thickness dependences, we get a comprehensive understanding of the TI underlayer influence on both the magnetic damping factor and magnetic anisotropy. It is found that the large RT damping enhancement in the TI/CoFe structure consists of both the spin pumping contribution stemming from the TI SSs and the MPE caused by magnetic coupling at the TI/FM interface. Moreover, we observe that the $4\pi M_{\text{eff}}$ value of Bi_2Te_3 /CoFe is 4.1 kOe lower than that of the single CoFe film grown directly on the SiO_2 substrate, suggesting an enhanced surface magnetic anisotropy induced by the Bi_2Te_3 underlayer. Further experiments verify that the observed strong $4\pi M_{\text{eff}}$ reduction mainly arises from the interfacial atomic intermixing, and the MPE contribution related to the TI SSs is rather weak. The temperature-dependent TR-MOKE study reveals that the damping arising from MPE increases with the decrease in temperature, whereas the surface magnetic anisotropy and additional damping induced by the topological SSs stay nearly unchanged. Our findings suggest an effective approach for

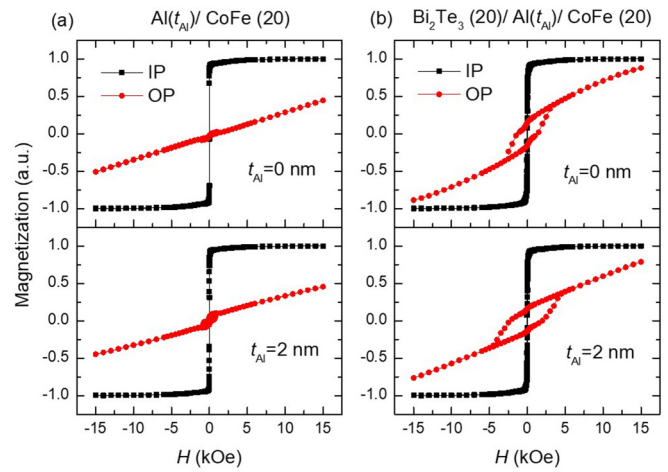


FIG. 6. The in-plane (IP) and out-of-plane (OP) hysteresis loops for samples of (a) $\text{SiO}_2/\text{Al}(t_{\text{Al}})/\text{CoFe}$ (20) and (b) $\text{SiO}_2/\text{Bi}_2\text{Te}_3$ (20)/ $\text{Al}(t_{\text{Al}})/\text{CoFe}$ (20).

the control of ultrafast magnetization dynamics in TI/NM/FM heterostructures with the unique properties of the SSs, which offers exciting opportunities for developing TI-based spintronics.

ACKNOWLEDGMENTS

This paper was supported by the National Natural Science Foundation of China (Grants No. 51671057, No. 11874120 and No. 12074072).

APPENDIX

We show here the IP and OP magnetic hysteresis loops measured by VSM.

- [1] H. Zhang, C. Liu, X. Qi, X. Dai, Z. Fang, and S. Zhang, Topological insulators in Bi_2Se_3 , Bi_2Te_3 and Sb_2Te_3 with a single Dirac cone on the surface, *Nat. Phys.* **5**, 438 (2009).
- [2] Y. Chen, J. Analytis, J. Chu, Z. Liu, S. Mo, X. Qi, H. Zhang, D. Lu, X. Dai, Z. Fang, S. Zhang, I. Fisher, Z. Hussain, and Z. Shen, Experimental realization of a three-dimensional topological insulator, *Science* **325**, 178 (2009).
- [3] H. Wang, J. Kally, J. Lee, T. Liu, H. Chang, D. Hickey, K. Mkhoyan, M. Wu, A. Richardella, and N. Samarth, Surface-State-Dominated Spin-Charge Current Conversion in Topological-Insulator-Ferromagnetic-Insulator Heterostructures, *Phys. Rev. Lett.* **117**, 076601 (2016).
- [4] N. Bansal, Y. Kim, M. Brahlek, E. Edrey, and S. Oh, Thickness-Independent Transport Channels in Topological Insulator Bi_2Se_3 Thin Films, *Phys. Rev. Lett.* **109**, 116804 (2012).
- [5] Y. Wang, D. Zhu, Y. Yang, K. Lee, R. Mishra, G. Go, S. H. Oh, D. H. Kim, K. Cai, E. Liu, S. D. Pollard, S. Shi, J. Lee, K. L. Teo, Y. Wu, K. J. Lee, and H. Yang, Magnetization switching by magnon-mediated spin torque through an antiferromagnetic insulator, *Science* **366**, 1125 (2019).
- [6] A. Taskin, S. Sasaki, K. Segawa, and Y. Ando, Manifestation of Topological Protection in Transport Properties of Epitaxial Bi_2Se_3 Thin Films, *Phys. Rev. Lett.* **109**, 066803 (2012).
- [7] Y. Zhang, K. He, C. Chang, C. Song, L. Wang, X. Chen, J. Jia, Z. Fang, X. Dai, W. Shan, S. Shen, Q. Niu, X. Qi, S. Zhang, X. Ma, and Q. Xue, Crossover of the three-dimensional topological insulator Bi_2Se_3 to the two-dimensional limit, *Nat. Phys.* **6**, 584 (2010).
- [8] J. Honolka, A. Khajetoorians, V. Sessi, T. Wehling, S. Stepanow, J. Mi, B. Iversen, T. Schlenk, J. Wiebe, N. Brookes, A. Lichtenstein, P. Hofmann, K. Kern, and R. Wiesendanger, In-Plane Magnetic Anisotropy of Fe Atoms on Bi_2Se_3 (111), *Phys. Rev. Lett.* **108**, 256811 (2012).
- [9] C. Li, O. van't Erve, J. Robinson, Y. Liu, L. Li, and B. Jonker, Electrical detection of charge-current-induced spin polarization due to spin-momentum locking in Bi_2Se_3 , *Nat. Nanotech.* **9**, 218 (2014).
- [10] J. Rojas-Sanchez, S. Oyarzun, Y. Fu, A. Marty, C. Vergnaud, S. Gambarelli, L. Vila, M. Jamet, Y. Ohtsubo, A. Taleb-Ibrahimi, P. Le Fevre, F. Bertran, N. Reyren, J. George, and A. Fert, Spin

- to Charge Conversion at Room Temperature by Spin Pumping into a New Type of Topological Insulator: α -Sn Films, *Phys. Rev. Lett.* **116**, 096602 (2016).
- [11] Y. Shiomi, K. Nomura, Y. Kajiwara, K. Eto, M. Novak, K. Segawa, Y. Ando, and E. Saitoh, Spin-Electricity Conversion Induced by Spin Injection into Topological Insulators, *Phys. Rev. Lett.* **113**, 196601 (2014).
- [12] A. Mellnik, J. Lee, A. Richardella, J. Grab, P. Mintun, M. Fischer, A. Vaezi, A. Manchon, E. Kim, N. Samarth, and D. Ralph, Spin-transfer torque generated by a topological insulator, *Nature* **511**, 449 (2014).
- [13] Y. Fan, P. Upadhyaya, X. Kou, M. Lang, S. Takei, Z. Wang, J. Tang, L. He, L. Chang, M. Montazeri, G. Yu, W. Jiang, T. Nie, R. Schwartz, Y. Tserkovnyak, and K. L. Wang, Magnetization switching through giant spin-orbit torque in a magnetically doped topological insulator heterostructure, *Nat. Mater.* **13**, 699 (2014).
- [14] J. Han, A. Richardella, S. Siddiqui, J. Finley, N. Samarth, and L. Liu, Room-Temperature Spin-Orbit Torque Switching Induced by a Topological Insulator, *Phys. Rev. Lett.* **119**, 077702 (2017).
- [15] N. H. D. Khang, Y. Ueda, and P. Hai, A conductive topological insulator with large spin Hall effect for ultralow power spin-orbit torque switching, *Nat. Mater.* **17**, 808 (2018).
- [16] Y. Wang, D. Zhu, Y. Wu, Y. Yang, J. Yu, R. Ramaswamy, R. Mishra, S. Shi, M. Elyasi, K. Teo, Y. Wu, and H. Yang, Room temperature magnetization switching in topological insulator-ferromagnet heterostructures by spin-orbit torques, *Nat. Commun.* **8**, 1364 (2017).
- [17] H. Wu, P. Zhang, P. Deng, Q. Lan, Q. Pan, S. A. Razavi, X. Che, L. Huang, B. Dai, K. Wong, X. Han, and K. Wang, Room-Temperature Spin-Orbit Torque from Topological Surface States, *Phys. Rev. Lett.* **123**, 207205 (2019).
- [18] M. De, R. Grassi, J. Chen, M. Jamali, D. R. Hickey, D. Zhang, Z. Zhao, H. Li, P. Quarterman, Y. Lv, M. Li, A. Manchon, K. Mkhoyan, T. Low, and J. Wang, Room-temperature high spin-orbit torque due to quantum confinement in sputtered $\text{Bi}_x\text{Se}_{(1-x)}$ films, *Nat. Mater.* **17**, 800 (2018).
- [19] H. Wu, Y. Xu, P. Deng, Q. Pan, S. Razavi, K. Wong, L. Huang, B. Dai, Q. Shao, G. Yu, X. Han, J. C. R. Sánchez, S. Mangin, and K. Wang, Spin-orbit torque switching of a nearly compensated ferrimagnet by topological surface states, *Adv. Mater.* **31**, 1901681 (2019).
- [20] Y. Wang, P. Deorani, K. Banerjee, N. Koirala, M. Brahlek, S. Oh, and H. Yang, Topological Surface States Originated Spin-Orbit Torques in Bi_2Se_3 , *Phys. Rev. Lett.* **114**, 257202 (2015).
- [21] P. King, R. Hatch, M. Bianchi, R. Ovsyannikov, C. Lupulescu, G. Landolt, B. Slomski, J. Dil, D. Guan, J. Mi, E. Rienks, J. Fink, A. Lindblad, S. Svensson, S. Bao, G. Balakrishnan, B. Iversen, J. Osterwalder, W. Eberhardt, F. Baumberger, and P. Hofmann, Large Tunable Rashba Spin Splitting of a Two-Dimensional Electron Gas in Bi_2Se_3 , *Phys. Rev. Lett.* **107**, 096802 (2011).
- [22] S. Shi, A. Wang, Y. Wang, R. Ramaswamy, L. Shen, J. Moon, D. Zhu, J. Yu, S. Oh, Y. Feng, and H. Yang, Efficient charge-spin conversion and magnetization switching through the rashba effect at topological-insulator/Ag interfaces, *Phys. Rev. B* **97**, 041115(R) (2018).
- [23] K. Kondou, R. Yoshimi, A. Tsukazaki, Y. Fukuma, J. Matsuno, K. Takahashi, M. Kawasaki, Y. Tokura, and Y. Otani, Fermi-level-dependent charge-to-spin current conversion by dirac surface states of topological insulators, *Nat. Phys.* **12**, 1027 (2016).
- [24] M. Jamali, J. Lee, J. Jeong, F. Mahfouzi, Y. Lv, Z. Zhao, B. Nikolic, K. Mkhoyan, N. Samarth, and J. Wang, Giant spin pumping and inverse spin Hall effect in the presence of surface and bulk spin-orbit coupling of topological insulator Bi_2Se_3 , *Nano Lett.* **15**, 7126 (2015).
- [25] C. Tang, Q. Song, C. Chang, Y. Xu, Y. Ohnuma, M. Matsuo, Y. Liu, W. Yuan, Y. Yao, J. Moodera, S. Maekawa, W. Han, and J. Shi, Dirac surface state-modulated spin dynamics in a ferromagnetic insulator at room temperature, *Sci. Adv.* **4**, eaas8660 (2018).
- [26] R. Sun, S. Yang, X. Yang, E. Vetter, D. Sun, N. Li, L. Su, Y. Li, Y. Li, Z. Gong, Z. Xie, K. Hou, Q. Gul, W. He, X. Zhang, and Z. Cheng, Large tunable spin-to-charge conversion induced by hybrid Rashba and Dirac surface states in topological insulator heterostructures, *Nano Lett.* **19**, 4420 (2019).
- [27] A. Nomura, N. Nasaka, T. Tashiro, T. Sasagawa, and K. Ando, Absorption of diffusive spin current in surface and bulk states of a topological insulator, *Phys. Rev. B* **96**, 214440 (2017).
- [28] Y. T. Fanchiang, K. H. M. Chen, C. C. Tseng, C. C. Chen, C. K. Cheng, S. R. Yang, C. N. Wu, S. F. Lee, M. Hong, and J. Kwo, Strongly exchange-coupled and surface-state-modulated magnetization dynamics in Bi_2Se_3 /yttrium iron garnet heterostructures, *Nat. Commun.* **9**, 223 (2018).
- [29] C. Lee, F. Katmis, P. Herrero, J. Moodera, and N. Gedik, Direct measurement of proximity-induced magnetism at the interface between a topological insulator and a ferromagnet, *Nat. Commun.* **7**, 12014 (2016).
- [30] M. Caminale, A. Ghosh, S. Auffret, U. Ebels, K. Ollefs, F. Wilhelm, A. Rogalev, and W. E. Bailey, Spin pumping damping and magnetic proximity effect in Pd and Pt spin-sink layers, *Phys. Rev. B* **94**, 014414 (2016).
- [31] W. E. Bailey, A. Ghosh, S. Auffret, E. Gautier, U. Ebels, F. Wilhelm, and A. Rogalev, Pd magnetism induced by indirect interlayer exchange coupling, *Phys. Rev. B* **86**, 144403 (2012).
- [32] Y. Sun, H. Chang, M. Kabatek, Y. Y. Song, Z. Wang, M. Jantz, W. Schneider, M. Wu, E. Montoya, B. Kardasz, B. Heinrich, S. G. te Velthuis, H. Schultheiss, and A. Hoffmann, Damping in Yttrium Iron Garnet Nanoscale Films Capped by Platinum, *Phys. Rev. Lett.* **111**, 106601 (2013).
- [33] Y. S. Hou and R. Q. Wu, Strongly Enhanced Gilbert Damping in 3d Transition-Metal Ferromagnet Monolayers in Contact with the Topological Insulator Bi_2Se_3 , *Phys. Rev. Appl.* **11**, 054032 (2019).
- [34] M. Lang, M. Montazeri, M. C. Onbasli, X. Kou, Y. Fan, P. Upadhyaya, K. Yao, F. Liu, Y. Jiang, W. Jiang, K. L. Wong, G. Yu, J. Tang, T. Nie, L. He, R. N. Schwartz, Y. Wang, C. A. Ross, and K. L. Wang, Proximity induced high-temperature magnetic order in topological insulator-ferrimagnetic insulator heterostructure, *Nano Lett.* **14**, 3459 (2014).
- [35] F. Katmis, V. Lauter, F. S. Nogueira, B. A. Assaf, M. E. Jamer, P. Wei, B. Satpati, J. W. Freeland, I. Eremin, D. Heiman, P. Jarillo-Herrero, and J. S. Moodera, A high-temperature ferromagnetic topological insulating phase by proximity coupling, *Nature* **533**, 513 (2016).
- [36] J. Kim, K. W. Kim, H. Wang, J. Sinova, and R. Wu, Understanding the Giant Enhancement of Exchange Interaction in Bi_2Se_3 -EuS Heterostructures, *Phys. Rev. Lett.* **119**, 027201 (2017).

- [37] M. Van Kampen, C. Jozsa, J. T. Kohlhepp, P. LeClair, L. Lagae, W. J. De Jonge, and B. Koopmans, All-Optical Probe of Coherent Spin Waves, *Phys. Rev. Lett.* **88**, 227201 (2002).
- [38] K. Cai, Z. Zhu, J. M. Lee, R. Mishra, L. Ren, S. D. Pollard, P. He, G. Liang, K. L. Teo, and H. Yang, Ultrafast and energy-efficient spin-orbit torque switching in compensated ferromagnets, *Nat. Electron.* **3**, 37 (2020).
- [39] J. Yoon, S. W. Lee, J. H. Kwon, J. M. Lee, J. Son, X. Qiu, K. J. Lee, and H. Yang, Anomalous spin-orbit torque switching due to field-like torque-assisted domain wall reflection, *Sci. Adv.* **3**, e1603099 (2017).
- [40] D. L. Zhang, J. Zhu, T. Qu, D. M. Lattery, R. H. Victora, X. Wang, and J. P. Wang, High-frequency magnetoacoustic resonance through strain-spin coupling in perpendicular magnetic multilayers, *Sci. Adv.* **6**, eabb4607 (2020).
- [41] J. Tang, Y. Ke, W. He, X. Zhang, W. Zhang, N. Li, Y. Zhang, Y. Li, and Z. Cheng, Ultrafast photoinduced multimode antiferromagnetic spin dynamics in exchange-coupled Fe/RFeO₃ ($R = \text{Er}$ or Dy) heterostructures, *Adv. Mater.* **30**, 1706439 (2018).
- [42] G. Wu, Y. Ren, X. He, Y. Zhang, H. Xue, Z. Ji, Q. Jin, and Z. Zhang, Tuning Magnetization Dynamics with Strong Spin-Orbit Coupling in Transition-Metal Dichalcogenide/Co-Fe-B Heterostructures, *Phys. Rev. Appl.* **13**, 024027 (2020).
- [43] G. Wu, S. Chen, Y. Ren, Q. Jin, and Z. Zhang, Laser-induced magnetization dynamics in interlayer-coupled [Ni/Co]₄/Ru/[Co/Ni]₃ perpendicular magnetic films for information storage, *ACS Appl. Nano Mater.* **2**, 5140 (2019).
- [44] M. Tang, B. Zhao, W. Zhu, Z. Zhu, Q. Jin, and Z. Zhang, Controllable interfacial coupling effects on the magnetic dynamic properties of perpendicular [Co/Ni]₅/Cu/TbCo composite thin films, *ACS Appl. Mater. Interfaces* **10**, 5090 (2018).
- [45] G. Wu, W. Zhu, Z. Zhu, H. Xue, Y. Ren, Y. Liu, Q. Jin, and Z. Zhang, Magnetic precession modes with enhanced frequency and intensity in hard/NM/soft perpendicular magnetic films, *Phys. Chem. Chem. Phys.* **21**, 16830 (2019).
- [46] A. Capua, S. Yang, T. Phung, and S. S. P. Parkin, Determination of intrinsic damping of perpendicularly magnetized ultrathin films from time-resolved precessional magnetization measurements, *Phys. Rev. B* **92**, 224402 (2015).
- [47] X. F. Kou, W. J. Jiang, M. R. Lang, F. X. Xiu, L. He, Y. Wang, Y. Wang, X. X. Yu, A. V. Fedorov, P. Zhang, and K. L. Wang, Magnetically doped semiconducting topological insulators, *J. Appl. Phys.* **112**, 063912 (2012).
- [48] C. Z. Chang, J. Zhang, M. Liu, Z. Zhang, X. Feng, K. Li, L. Wang, X. Chen, X. Dai, Z. Fang, X. L. Qi, S. C. Zhang, Y. Wang, K. He, X. C. Ma, and Q. K. Xue, Thin films of magnetically doped topological insulator with carrier-independent long-range ferromagnetic order, *Adv. Mater.* **25**, 1065 (2013).
- [49] B. Khodadadi, J. B. Mohammadi, J. M. Jones, A. Srivastava, C. Mewes, T. Mewes, and C. Kaiser, Interlayer Exchange Coupling in Asymmetric Co-Fe/Ru/Co-Fe Trilayers Investigated with Broadband Temperature-Dependent Ferromagnetic Resonance, *Phys. Rev. Appl.* **8**, 014024 (2017).
- [50] A. Kumar, R. Gupta, S. Husain, N. Behera, S. Hait, S. Chaudhary, R. Brucas, and P. Svedlindh, Spin pumping and spin torques in interfacially tailored Co₂FeAl/ β -Ta layers, *Phys. Rev. B* **100**, 214433 (2019).
- [51] H. Lee, L. Wen, M. Pathak, P. Janssen, P. LeClair, C. Alexander, C. K. A. Mewes, and T. Mewes, Spin pumping in Co₅₆Fe₂₄B multilayer systems, *J. Phys. D* **41**, 215001 (2008).
- [52] Z. Zhu, S. Chen, B. Zhao, Q. Jin, J. Chen, and Z. Zhang, Control of perpendicular magnetic anisotropy and spin pumping damping in MgO/CoFeB/Ta/Pt structures, *J. Phys. D* **50**, 355001 (2017).
- [53] N. Behera, S. Chaudhary, and D. K. Pandya, Anomalous anti-damping in sputtered β -Ta/Py bilayer system, *Sci. Rep.* **6**, 19488 (2016).
- [54] A. J. Schellekens, K. C. Kuiper, R. R. de Wit, and B. Koopmans, Ultrafast spin-transfer torque driven by femtosecond pulsed-laser excitation, *Nat. Commun.* **5**, 4333 (2014).
- [55] Y. D. Glinka, S. Babakiray, T. A. Johnson, A. D. Bristow, M. B. Holcomb, and D. Lederman, Ultrafast carrier dynamics in thin-films of the topological insulator Bi₂Se₃, *Appl. Phys. Lett.* **103**, 151903 (2013).
- [56] L. Luo, X. Yang, X. Liu, Z. Liu, C. Vaswani, D. Cheng, M. Mootz, X. Zhao, Y. Yao, C. Z. Wang, K. M. Ho, I. E. Perakis, M. Dobrowolska, J. K. Furdyna, and J. Wang, Ultrafast manipulation of topologically enhanced surface transport driven by mid-infrared and terahertz pulses in Bi₂Se₃, *Nat. Commun.* **10**, 607 (2019).
- [57] G. Chai, N. N. Phuoc, and C. K. Ong, Optimizing high-frequency properties of stripe domain ferrite doped CoFe thin films by means of a Ta buffer layer, *J. Phys. D* **46**, 415001 (2013).
- [58] B. Cui, C. Song, Y. Y. Wang, W. S. Yan, F. Zeng, and F. Pan, Tuning of uniaxial magnetic anisotropy in amorphous CoFeB films, *J. Phys. Condens. Matter* **25**, 106003 (2013).
- [59] Y. Li, F. Zeng, S. S. Zhang, H. Shin, H. Saglam, V. Karakas, O. Ozatay, J. E. Pearson, O. G. Heinonen, Y. Wu, A. Hoffmann, and W. Zhang, Giant Anisotropy of Gilbert Damping in Epitaxial CoFe Films, *Phys. Rev. Lett.* **122**, 117203 (2019).
- [60] Z. Zhu, G. Wu, Y. Ren, S. Lou, Q. Jin, and Z. Zhang, Modulation of magnetic damping in antiferromagnet/CoFeB heterostructures, *Appl. Phys. Lett.* **116**, 182407 (2020).
- [61] S. Azzawi, A. Ganguly, M. Tokaç, R. M. Rowan-Robinson, J. Sinha, A. T. Hindmarch, A. Barman, and D. Atkinson, Evolution of damping in ferromagnetic/nonmagnetic thin film bilayers as a function of nonmagnetic layer thickness, *Phys. Rev. B* **93**, 054402 (2016).
- [62] E. Barati, M. Cinal, D. M. Edwards, and A. Umerski, Gilbert damping in magnetic layered systems, *Phys. Rev. B* **90**, 014420 (2014).
- [63] X. Wang, L. Cheng, D. Zhu, Y. Wu, M. Chen, Y. Wang, D. Zhao, C. B. Boothroyd, Y. M. Lam, J. X. Zhu, M. Battiato, J. C. W. Song, H. Yang, and E. E. M. Chia, Ultrafast spin-to-charge conversion at the surface of topological insulator thin films, *Adv. Mater.* **30**, 1802356 (2018).